JOURNAL OF GEOPHYSICAL RESEARCH, VOL. ???, XXXX, DOI:10.1029/,

Quantifying irreversible mixing during baroclinic wave life cycles: the influence of stratospheric stratification and turbulent diffusivity

Y. H. Yamazaki

Atmospheric, Oceanic and Planetary Physics, University of Oxford, UK

W. R. Peltier

Department of Physics, University of Toronto, CANADA

Y. H. Yamazaki, Atmospheric, Oceanic and Planetary Physics, Clarendon Laboratory, University of Oxford, Parks Road, OXFORD, OX1 3PU, U.K. (hiro@atm.ox.ac.uk)

W. R. Peltier, Department of Physics, University of Toronto, 60 St George Street, Toronto, Ontario, M5S 1A7, CANADA (peltier@atmosp.utoronto.ca)

Abstract. To assess the significance of small-scale non-isentropic mixing processes associated with the nonlinear evolution of synoptic-scale baroclinic waves in mid-latitudes, we have employed a dry anelastic model and executed a series of three-dimensional numerical simulations which explicitly resolve the secondary structures that develop in both the troposphere and lower stratosphere such as intense surface fronts and tropopause folds. We first demonstrate that the stratospheric stratification has little influence on the structure and amplitude of the descending tropopause folds and that the assumed strength of the small-scale turbulence has only minor influence in the PV structure in the lower stratosphere and upper troposphere, although it has a striking impact on the surface front. We then quantify the degree of non-isentropic irreversible mixing in these life cycles as a function of time by computing the evolution of the "base" or "unavailable" component of potential energy to find that the most intense mixing occurs in the saturation stage of the life cycle but that the irreversible change of energy due to mixing remains only a few percent of that due to stirring in all cases. The evolution of the thermodynamic entropy is also employed as an alternative measure of non-isentropic mixing, and both temporal and spatial distributions of mixing activity are quantified. We confirm that the surface fronts are the most active regions of mixing, followed by the fluid in the vicinity of the descending tropopause.

1. Introduction

Knowledge of the extent and importance of irreversible mixing processes is clearly essential to understanding the high Reynolds number flow of a stratified fluid. Both the atmosphere and oceans of Earth are strongly stratified and naturally support a variety of phenomena through which mixing is engendered. One of the most fully-investigated of such natural processes and one that has a striking impact on the general circulation of the atmosphere is the process of baroclinic wave evolution at the synoptic scale. Whereas the dominant mechanism underlying the initial exponential growth of synoptic-scale waves is well-explained by inviscid linear instability theories such as the classical quasi-geostrophy based analyses of Charney (1947) and Eady (1949), the mechanisms of nonlinear saturation and decay are still under active investigation. These phases of wave evolution involve both large-scale processes related to wave mean-flow interaction and meso-scale processes including the generation of both localized secondary instabilities and the excitation of internal gravity waves through "imbalance". Even smaller-scale processes involving strong dissipation and irreversible mixing will inevitably be induced by such baroclinic-wave life cycles. Examples of subsynoptic-scale structural features that typically form during the nonlinear evolution of synoptic-scale waves are those known as fronts and tropopause folds, both of which are likely to engender meso-scale and micro-scale processes in regions in which the temperature and velocity fields develop strong spatial gradients and which, by occurring, prevent the development of spatial singularities in these otherwise adiabatic non-dissipative fields.

One of the goals of this paper is to identify the morphological indications of irreversible mixing and to estimate the importance of such subsynoptic-scale processes that emerge during the nonlinear evolution of a synoptic-scale disturbance. In particular, we will examine the influence of the stratification contrast between stratosphere and troposphere, and of the assumed strength of the turbulent diffusivity. The dynamical and thermodynamical framework of the analyses to be presented herein, as with the previous work of Polavarapu and Peltier (1990, hereafter PP), Bush and Peltier (1994, hereafter BP), and Yamazaki and Peltier (2001, hereafter YP) is a non-hydrostatic model based upon the anelastic approximation, which can accurately simulate the various meso-scale features of interest.

A further goal will be to quantitatively describe the degree of non-isentropic irreversible mixing that is associated with deformations of the surface fronts and tropopause by employing rigorous measures of this process. Of primary interest for the work to be discussed herein is a methodology with which one may measure the degree of irreversible mixing that occurs during the evolution of a stratified fluid as a function of time and space.

Recently, Nakamura (1996) proposed one such convenient measure of mixing. His idea is that the mixing rate can be estimated by the equivalent length of an appropriate tracer contour multiplied by a diffusion coefficient. This measure is especially useful when the diffusivity is uniform and isotropic, and it can indeed be employed to describe the spatial distribution of the mixing rate. However, in principle, the diffusivity ought to represent all of the "unresolved" processes that occur on the diffusion-scale and the magnitude of this effective diffusivity is not easy to obtain. For example, in numerical models of the atmosphere, implicit (and explicit) diffusivity is inevitably incorporated due to the model

numerics, especially where temporal or spatial gradients are large and the magnitude of the implicit diffusivity is difficult to estimate. The situation is also complex in observational studies because data are "sampled" in time and space and the evolution of the effective diffusivity is most difficult to follow. In short, in a moderately complex system such as a planetary fluid, the effective diffusivity is a function of time, space, and "sampling" resolution and cannot be determined on an *a priori* basis.

One way to quantify the temporal evolution of mixing may be accomplished by following the original analysis by Margules (1903), who defined a partition of the potential energy into two subcomponents which respectively can and cannot be converted into kinetic energy (see Gill, 1982). Later, Lorenz (1955) clarified the meaning of these energy components and established the concept of available potential energy (APE hereafter) and minimal potential energy (we will refer to the latter as "base" potential energy or BPE). The latter can be understood as the base part of the potential energy that reflects only the thermodynamic state of the entire fluid system. The concepts of BPE and APE were recently employed by Winters *et al.* (1995) to quantitatively diagnose the degree of diapycnal mixing that occurs in a shear flow undergoing two-dimensional Kelvin-Helmholtz instability. More recently, Caulfield and Peltier (2000, hereafter CP) have generalized this analysis and diagnosed the evolution of irreversible mixing during the three-dimensional "life cycle" of a stratified shear flow. A detailed summary of this work has recently appeared in Peltier and Caulfield (2003) in which the methodology has enabled the authors to provide a definitive demonstration of the fact that turbulence may act in an antidiffusive fashion upon the mixing of an initial density stratification.

In this paper, we will initially employ the same methodology. The procedure developed by Winters *et al.* and CP for application to understanding the irreversible mixing for an incompressible fluid will be extended so as to apply to the more atmospherically realistic anelastic fluid models characterized by either isentropic or non-isentropic reference states. In addition, an alternative methodology for the analysis of irreversible mixing will be proposed. We will demonstrate herein that the evolution of classical thermodynamic entropy is closely related to the evolution of BPE and define an "irreversible activity index" to diagnose the temporal and spatial localization of irreversible processes.

After a brief description of our model in Section 2, the results of a series of numerical simulations of baroclinic-wave life cycles will be presented in Section 3. The energy-based diagnosis employed to quantify irreversible non-isentropic mixing will then be discussed and applied in Section 4. The entropy-based analysis will be employed in Section 5 to describe the mixing activities in both time and space. Our results are summarized in Section 6. The details of the procedure we have developed for calculating base potential energy in anelastic models is described in the Appendix.

2. Model

The numerical model to be employed for all of the analyses reported herein is based upon an implementation of the equations describing a non-hydrostatic anelastic fluid. The governing equations were discretized using second order accurate centered finite differences, as described in Clark (1977). In a rotating Cartesian coordinate system $\boldsymbol{x} = (x, y, z)$ with x increasing eastward, y northward, and z upward, the governing equations can be

written as

$$\frac{\mathrm{D}\,\boldsymbol{u}}{\mathrm{D}\,t} + \boldsymbol{f} \times \boldsymbol{u} = -\boldsymbol{\nabla}\frac{p_1}{\rho_0} - \frac{\theta_1}{\theta_0}\boldsymbol{g} + \boldsymbol{F}, \tag{1}$$

$$\frac{c_p}{\theta_0}\frac{\mathrm{D}\,\theta}{\mathrm{D}\,t} = \frac{Q}{T_0}, \tag{2}$$

$$\boldsymbol{\nabla} \bullet (\rho_0\,\boldsymbol{u}) = 0. \tag{3}$$

in which $\boldsymbol{u} = (\ u(\boldsymbol{x},t),\ v(\boldsymbol{x},t),\ w(\boldsymbol{x},t)\ )$ is three-dimensional velocity vector, $p = p(\boldsymbol{x},t)$ is pressure, $\theta = \theta(\boldsymbol{x},t)$ is potential temperature, $\rho = \rho(\boldsymbol{x},t)$ is density, $T = T(\boldsymbol{x},t)$ is absolute temperature, and c_p is specific heat capacity. The vector $\boldsymbol{F}$ denotes the frictional force per unit mass, while the scalar Q denotes the rate of heating due to turbulent diffusivity. The vector $\boldsymbol{f} = (0, 0, f)$ is the Coriolis parameter and $\boldsymbol{g} = (0, 0, -g)$ is the gravitational acceleration. The values of f and g are set equal to 10^{-4} s^{-1} and 9.81 m s^{-2} respectively.

The subscript 0 denotes a corresponding quantity in the reference state, all of which are functions of height only, whereas the subscript 1 denotes a deviation from the reference state. The reference state is assumed to be motionless and isentropic.

We will be obliged to consider two sources of dissipation in the numerical model, one due to the numerical methodology, $\boldsymbol{F_N}$, and the other due to the explicit turbulence parameterization, $\boldsymbol{F_T}$. Hence we have

$$\boldsymbol{F} \triangleq \boldsymbol{F_N} + \boldsymbol{F_T}. \tag{4}$$

The friction arising from the numerical methodology, $\boldsymbol{F_N}$, is introduced primarily to ensure numerical stability and the mathematical forms selected for the numerical viscosity may be classified into three groups: namely those having $\boldsymbol{\nabla}_H^6$, $\boldsymbol{\nabla}_H^4$, and $\boldsymbol{\nabla}_H^2$ dependencies, where $\boldsymbol{\nabla}_H^2$ denotes the horizontal Laplacian operator. The numerical viscosity of $\boldsymbol{\nabla}_H^6$ type

is employed over the entire domain of calculation except for a few grid-planes near the north and south walls, where the lower order diffusion operators are applied.

The explicit parameterization of friction that is intended to represent the influence of unresolved "turbulence" at the subgrid scale is $\boldsymbol{F_T}$. We employ a three-dimensional version of the first-order closure discussed by Lilly (1962). The turbulent mixing coefficient, K_m, is a function of an external constant called the "eddy viscosity parameter" K_c, the deformation Def, and the local gradient Richardson number, Ri^*, as

$$K_m \triangleq \begin{cases} K_c\, Def\, (1 - Ri^*)^{\frac{1}{2}}, & Ri^* < 1; \\ 0, & \text{otherwise.} \end{cases} \tag{5}$$

The eddy Prandtl number for the turbulence parameterization is assumed to be unity and there is no parameterized boundary layer near the surface. We employ a free-slip boundary condition at the bottom of the simulation domain for simplicity.

The energetics may be summarized as follows:

$$\frac{d}{dt}TKE = +[VHF] - [DIS], \tag{6}$$

$$\frac{d}{dt}TPE = -[VHF] - [DIF], \tag{7}$$

$$\frac{d}{dt}ZKE = -[VRS] - [HRS] - [DIS_Z], \tag{8}$$

$$\frac{d}{dt}EKE = +[VHF] + [VRS] + [HRS] - [DIS_E], \tag{9}$$

where [ ] denotes the domain average. The energy components *TKE* and *TPE* are total kinetic energy and total potential energy respectively, and *ZKE* and *EKE* are zonal-mean and eddy components of kinetic energy. The energy conversion terms on the right hand sides of the equations are vertical heat flux (*VHF*), vertical Reynolds stress (*VRS*), horizontal Reynolds stress (*HRS*), dissipation (*DIS*), and diffusion (*DIF*). The dissipation

is partitioned into the zonal-mean and eddy components (DIS_Z and DIS_E) and the total energy due to dissipation will be lost from the system.

For the purpose of the analyses to be presented herein, we will employ three primary initial flows in a cyclic channel, each of which consists of modeled troposphere and stratosphere with different degrees of stratification, as displayed on Fig.1 and Fig.2. The flow fields of the control case shown in Fig.1 were constructed to represent a realistic midlatitude jet stream observed in wintertime in the Western Pacific as described in YP. The strength of the stratification of the stratosphere is controlled by a parameter that we will refer to as the "stratification contrast", S_C, as

$$N_S{}^2 \triangleq S_C \; N_T{}^2, \tag{10}$$

where N_S denotes the buoyancy frequency of the stratosphere and N_T denotes that of the troposphere ($N_T \equiv 10^{-2}$ s^{-1} for the present applications). The channel length, width, and height are taken to be 4000 km, 8000 km, and 18 km respectively. Also employed is an initial flow with a rigid lid at the model tropopause ($z = 9$ km), which is expected to represent the case with infinitely large stratification contrast.

We will also discuss some aspects of results from simulations with two additional initial flows in the same channel geometry as the control: one with reduced baroclinicity (similar to the climatological zonal mean) in Section 3.1.1 and the other with slightly reduced stratospheric stratification (Sc=4) in Section 4.

For all cases, the potential temperature distribution is assumed to be independent of the zonal (x) coordinate and defined by an analytical expression in the y-z plane, whereas the velocity is set to zero on the ground and is in thermal wind balance with the potential temperature distribution. The definition of the initial mean flow is basically the same as

those employed by BP and YP. In fact, they are identical unless S_C is less than 6. In the present model, the definition of tropopause height, $h_T(y)$, is replaced by

$$h_T(y) \equiv h_0 \; - \frac{g}{\max({N_S}^2,\; 6{N_T}^2) - {N_T}^2} \frac{\theta_J}{\theta_c} \tanh\left\{ \frac{(y - y_c)\, w_J^{-1}}{Y_J} \right\}, \tag{11}$$

in the notation of YP. The cross-frontal change of tropopause height takes the maximum value of 1.062 km when S_C is equal to or less than 6, and decreases monotonically as S_C increases above 6.

3. Overview of simulated life cycles

We have carried out 6 primary numerical experiments, the conditions for which are summarized in Table 1. The experiments may be seen to separate into two groups: namely those designed to test the influence of the stratification contrast (S_C), and those designed to test the influence of the assumed strength of the subgrid-scale turbulence (K_c).

All of the parameters of the control run, labeled Control, are the same as those of the synoptic-scale simulation reported in YP, although for the purpose of the present study we have developed a more accurate method for calculating the initial state of balance. The time step was 90 seconds and the numerical grid spacings were DX = 62.5 km in the along-front direction, DY = 63.5 km in the cross-front direction, and DZ = 310 m in the vertical direction. No turbulence parameterization was incorporated in Control and there was no disturbance explicitly superimposed upon the balanced initial fields. A small-amplitude baroclinic disturbance inevitably develops out of the truncation error and assumes the optimal modal structure.

In order to examine the dependence of the baroclinic wave life cycle on the strength of upper level stratification, we have performed two comparison analyses labeled HighNs

and LowNs, which respectively employ more and less strongly stratified stratospheres as noted in Table 1. The initial fields for these runs have been illustrated in Fig.2. On physical grounds, it would be reasonable to expect that a different degree of upper level stratification will lead to a different degree of tropopause deformation because this property relates to the effective "rigidity" of the tropopause interface.

The cases Eddy1 and Eddy2 are the same as Control except that the turbulence parameterization is activated at different strengths. As discussed by Lilly (1962), the external eddy viscosity parameter, K_c, can be interpreted to be determined by the choice of characteristic grid size $\triangle$ and the Kolomogorov number k_K as $K_c = (k_K \triangle)^2$, where $\triangle = (DX\, DY\, DZ)^{\frac{1}{3}}$. In the viscous simulations, the Kolomogorov numbers that correspond to Eddy1 and Eddy2 are approximately 0.0009 and 0.003 respectively. Thus, the parameterized eddy mixing effects can be considered "weak" for both cases.

3.1. The control run

In this section, the general features of the life cycle that is simulated by our control run, Control, will be briefly summarized. Since an almost identical case has already been described in YP, the discussion herein will be restricted to the characteristics of the flow in the nonlinear stage of the life cycle, primarily forcusing on the morphorological features of active mixing.

3.1.1. Energetics

The evolution of Control is summarized in terms of its energetics in Fig.3. For the first 9 days, the "formation" of a normal mode disturbance takes place, followed by "exponential growth". The growth rate decreases in the "saturation" period from day 13.5 to day 15 and the period of "decay" lasts from day 15 to day 17.5.

The evolution is essentially identical to the results described in YP except that we are now able to recognize an even earlier phase of the exponential growth at smaller amplitude due to the improvements in the procedure for obtaining the balanced initial state. Unlike the initial fields employed by PP, BP and YP, the temperature field for the present study is calculated from the analytical definition at the desired resolution while the velocity field is directly calculated by an accurate discrete implementation of thermal wind balance on staggered grids without iterative modification. This level of care is required because the conventional figures concerning the energy exchanges are often misleading. One important point we wish to draw attention to in Fig.3 is that the initiation and termination of exponential growth occur at day 9 and day 13 respectively. This is evident from the evolution of growth rate but is impossible to discern on the basis of more conventional diagrams such as that of Fig.3a.

The initial fields of conventional life cycle simulations are not well balanced due to the presence of a superimposed disturbance. This makes the analysis of the termination of the exponential growth stage and of the initial stage of saturation difficult, simply because the stage of truly "exponential" growth is hard to identify (e.g., BP). The first stage of nonlinear saturation (i.e., from the termination of exponential growth to the beginning of decay) is characterized by the saturation of the positive energy terms themselves (VHF and VRS) which no longer grow exponentially from day 13.5 to day 15. In the evolution of the energy conversion terms shown in Fig.3b, the beginning of the saturation period coincides with the emergence of a positive impulse of HRS. In other words, the onset of saturation is not due to the onset of barotropic decay; it is rather associated with the impulse of barotropic "growth".

The spatial distribution of the energy conversion terms is displayed in Fig.4 at the beginning and the end of the impulse of positive HRS. Clearly, the apparent absence of a purely barotropic energy conversion through HRS until day 13 is not only due to the small magnitude of the barotropic conversion but is also due to the cancellation of simultaneous conversions with positive and negative sign as seen in Fig.4c. In other words, bartropic growth and decay of eddy energy occur simulataneously on both sides of the front during the exponential development of the baroclinic wave. However, the region of negative HRS diminishes by day 13.5 and the positive impulse of the barotropic energy conversion dominates in the total HRS as shown in Fig.4f.

The shallow, surface-confined regions of active HRS in Fig.4c and Fig.4f appeared in the nonlinear stage. The localized regions with positive and negative HRS below 2 km do not exist until day 12 (not shown in figure), although the spatial structure of the energy conversion terms during the exponentially growing stage is almost identical to that at day 12.75 except for this surface feature. This development of the surface-confined disturbance is the earliest indication of the emergence of a deep disturbance that eliminates the region of negative HRS in the middle and upper troposphere. In this sense, the localized breakdown, or "rupture", of the surface front at its northern extrema, which we will see in the following section, can be understood as an early indication of the emergence of a deep structure that eliminates the region of negative HRS.

3.1.2. Evolution of the surface front

The evolution of the surface potential temperature field is displayed in Fig.5f–j as a time series of planform snapshots. Despite the absence of the initially superimposed disturbance, a normal mode disturbance with zonally-sinusoidal structure initially develops.

The strong influence of nonlinear effects becomes clearly evident by day 13.75 with the formation of a cusp near the "rupture" point of the frontal structure. The cusp develops until approximately day 15.75 when it is detached from the front.

It may be worth noting that the classical occlusion process is not observed in these results in the sense that the cold front never "collides" with the warm front to isolate a region of occluded air. Instead, following a localised breakdown of the front at the northern extrema, a "seclusion" of relatively warm air begins to form in the cold side of the front and an intense cyclic spiral of intertwined fingers of warm and cold air thereafter develops. This result is similar to that of PP and supports the new view of the nonlinear development of baroclinic waves discussed by Shapiro and Keyser (1990) and Neiman, Shapiro and Fedor (1993).

3.1.3. Upper level cyclogenesis

Isentropic PV maps on the $\theta = 325$ K surface are employed to diagnose the features associated with upper level cyclogenesis. This surface is initially located just above the tropopause and goes through the core of the jet as shown in Fig.1. Note however that the isentropic surface deforms considerably and becomes "wavy" by day 14.

The evolution of the PV field on this isentropic surface is shown in Fig.5a–e. A weak sinusoidal variation of an initially parallel structure becomes visible by day 11, and the wavy pattern becomes clearly non-symmetric by day 12.5. At about day 13.5, a small region of high PV appears to the north of the front near the western boundary of the simulation domain, as seen in Fig.5b. This is associated with the barotropic rupture as is clear on the basis of Fig.3b and Fig.4. The signature of the barotropic event, which was illustrated in Fig.4, is evident by comparing Fig.5b and Fig.5g.

As the synoptic-scale wave becomes intense and the development strongly nonlinear, an elongated strip of PV begins to evolve into a beautifully articulated spiral structure in our f-plane model. The evolution of this spiral structure was first clearly resolved in the analyses of PP and has recently been investigated in detail by Methven and Hoskins (1998) and Methven (1998).

3.1.4. Tropopause deformation

The tropopause can be approximately represented by the isosurface on which potential vorticity (PV) is unity as in the cases examined by BP. This surface does not exactly overlay the tropopause at the center of the jet and slightly penetrates into the lower stratosphere as seen in Fig.1. Nevertheless, the surface reasonably represents the initial tropopause and the conservative property of PV in adiabatic inviscid flow implies that by observing the deformation of this isosurface we may effectively visualize the deforming tropopause without having to explicitly introduce a field of passive tracers.

Two examples of the three-dimensional structure of the tropopause, which is defined by this isosurface, are visualized in Fig.6. The figure clearly shows the complexity of the three-dimensional structure of this isosurface. The isosurface rendering in this figure actually shows one surface that represents the deformed tropopause and another that shows the region of high PV which is generated near the bottom boundary. Until day 14.25, the deformed tropopause can easily be distinguished from the surface of boundary-generated PV. However, by day 15.75, the descending tropopause apparently intertwines with the ascending surface of boundary-generated PV, and it becomes impossible to distinguish between the two isosurfaces solely by inspecting the structure from a few points of view.

For example, we had to examine several cross sections for day 15.75 to actually tell that the two major isosurfaces shown in Fig.6b are separated.

It is clear that the analysis of a rendered isosurface is not a suitable means by which to perform quantitative comparison of the degree of tropopause deformation and we will thus diagnose the structure of the deformed tropopause primarily on cross sections of the PV field along the center of the initial jet (at $y = 4000$ km). The evolution of the nonlinear wave in terms of a selected set of such PV cross sections is displayed in Fig.7. Illustrated in Fig.7a is the PV structure of the nonlinear wave that exists when the amplitude of the "synoptic-scale deformation" of the tropopause has obtained its maximum expression. The non-symmetric shape of the synoptic-scale deformation reveals some evidence of upper level saturation by day 13.75 in the form of a broad basin-shaped depression of the tropopause. It is interesting to note that the saturation of the upper level deformation of the "lid" coincides in time with the saturation of the impulse of positive barotropic conversion of energy. Meanwhile, the underside of the synoptic-scale deformation, which is defined as the lower convex ceiling of the troposphere at this stage, is visible near $x = 3700$ km. The amplitude of the synoptic-scale deformation can be measured as the difference between upper and lower ceilings.

Aside from the large horizontal-scale deformation of the tropopause, these figures also reveal the continuing descent of stratospheric air in a small-scale "fold" (see Fig.7b,c), as well as the development of secondary folds associated with the spiral structure of the main vortex (Fig.7c). Structures very similar to these are, of course, observed in nature (e.g., Danielsen and Hipskind, 1980) as previously discussed by BP, but we must remember that Fig.7c shows only a single cross section through what is in fact the complex three-

dimensional structure of tropopause deformation shown previously in Fig.6. The final PV structure shown in Fig.7d for day 18.5 is smoother in the troposphere, but more fragmented in the stratosphere.

3.2. The influence of the stratification contrast

The influence of the varying stratification contrast between stratosphere and troposphere, S_C, will be investigated in this section by examining the simulated life cycles in flows with different degrees of upper level stratification. The authors are not aware of similar analyses in the literature.

3.2.1. Energetics

The energetics of the LowNs, HighNs, and RigidLid simulations are summarized in Fig.8. For all cases, results are similar to those obtained in Control. In particular, the growth rate in the exponential stage is essentially independent of the variation in the stratification contrast. The similarity is understandable on the basis of the spatial distribution of the energy conversions during the exponentially growing stage which occur almost entirely in the troposphere even when the stratification contrast S_C is reduced.

Closer inspection of the energetics does, however, allow us to identify a number of differences. The most notable difference concerns the level of the zonal kinetic energy in the saturated state, which decreases as the stratification contrast increases. Another recognizable difference concerns the fast oscillatory change of the energy conversion terms. The amplitude and the period of this variation are very sensitive to the stratification contrast and the oscillatory variation is clearest in the case of HighNs (Fig.8e). A similar oscillatory variation is also evident in the result from Control shown in Fig.3.

3.2.2. Deformation of the tropopause

Examination of the potential vorticity structures delivered by these simulations immediately leads to identification of the most significant differences in the degree of upward penetration of the tropopause at the synoptic-scale. Shown in Fig.9a–b are the vertical cross sections of the potential vorticity fields when the amplitude of the synoptic-scale deformation, defined in Section 3.1.4, is maximum.

The maximum amplitude of the synoptic-scale deformation of the tropopause increases as the stratification contrast S_C is reduced from that of the control run as expected. The influence of increased stratification contrast is very minor because the amplitude of the synoptic-scale deformation is already small for the realistic case of Control.

Meanwhile, the maximum degree of descent of the subsynoptic-scale tropopause folds may be diagnosed on Fig.9c–d. Despite the strong dependence of the synoptic-scale deformation on the stratification contrast in Fig.9a–b, the behaviour of the small-scale folds is practically insensitive to the change of the stratification contrast. In fact, the small-scale PV structure in the troposphere below 9 km in height is almost identical for all cases, although the PV structure is completely different in the stratosphere.

3.3. Influence of the strength of subgrid-scale turbulence

The influence of the assumed level of subgrid-scale turbulence on these simulations has been investigated by changing the eddy viscosity parameter K_c in the turbulence parameterization. In this section, the influence will be examined on the basis of conventional diagnoses of the model fields. More significant differences will later be evaluated through the mixing analyses in Section 4 and Section 5.

As discussed in Section 2, the turbulent mixing coefficient, K_m, is a function of both time and space. Shown in Fig.10 is the evolution of the spatial maximum of the field K_m

for cases Eddy1 and Eddy2. Until day 12.375, the turbulent effects remain identically zero because the local Richardson number has remained in excess of unity in the entire domain. The initial impulse of strong mixing at day 13.5 corresponds to the time of onset of positive horizontal Reynolds stress. This supports the hypothesis that the frontal fracture accompanies a strong increase in diffusivity. Moreover, the very noisy evolution for the entire period suggests that there exist numerous mixing events which are short-lived and, most probably, highly localized. Nevertheless, we see no major differences in the basic energetics of Control, Eddy1 and Eddy2.

3.3.1. Upper and lower level cyclogenesis

The evolution of the surface potential temperature field is, in general, similar for all cases with different levels of subgrid-scale turbulence. The evolution of Eddy2 is displayed in Fig.11f–j which can be compared with Fig.5f–j. The similarity includes the meso-scale features such as "multiple fronts" that can be identified as the parallel structure along both warm and cold fronts that is most clearly seen at days 14.75 and 15.75.

Nevertheless, in the evolution of Eddy2, a clear sign of more intense mixing becomes apparent along the fronts by day 15.75, subsequent to which the fronts become more diffuse. The first sign of such mixing along the warm front appeared around day 15 as the emergence of periodic structure that is perpendicular to the front. We found that the Richardson number of this region is less than 0.25. This suggests the occurrence of Kelvin-Helmholtz instability, although it is only marginally resolved in our numerical model. The mature cold front shown in Fig.11j is not smooth but rather wavy.

Despite the marked difference at the surface, the evolution of the upper level cyclogenesis diagnosed on the isentropic PV maps is almost identical for all cases with different levels of parameterized diffusion. Examples are presented in Fig.11a–e for Eddy2.

3.3.2. Vertical structure of PV

The evolution of the vertical cross section of PV is displayed in Fig.12 and is generally similar to that for Control shown in Fig.7. The maximum level of synoptic-scale deformation of the tropopause at day 13.75 (Fig.12a) is identical to that of Control ($S_C = 6$) shown in Fig.9. At day 14.25 (Fig.12b), when the degree of tropopause descent reaches the initial temporal maximum, the region of strong PV gradient in the stratosphere near $(x, z) \approx$ (3000 km, 12 km) shows a sign of "wrinkles" or "ripples" with large amplitude. An investigation of the horizontal structure revealed that the wrinkles run primarily parallel to the jet streak, supporting the possible occurence of a symmetric instability. The effects of increased viscosity are evident near the surface. The region of high PV along the front is weaker in Eddy2 than in Control.

At day 15.75 (Fig.12c), when the descent of the folds reaches the secondary temporal maximum, the small-scale PV structure in the troposphere is slightly but significantly smoother than that of Control and thus shows signs of irreversible mixing having occurred. The final PV structure at day 18.5 (Fig.12d), compared with that from Control, shows a stronger influence of tropospheric mixing, although most of the fine structure in the stratosphere remains unaffected.

4. Energy-based diagnosis of irreversible mixing

In this section, in order to quantify the extent of irreversible mixing that occurs during the development of a typical baroclinic wave, we will first discuss the concept of mixing

rate, the definition of which is based upon the concept of "base potential energy". The actual procedure to be employed for calculating BPE will be described in Section 4.2. The suite of simulated life cycles will then be diagnosed using the measure of irreversible mixing to be discussed in Section 4.3. It will be important to understand that our focus in all that follows will be upon mixing of the potential temperature field, which is equivalent to "diapycnal mixing", under the anelastic approximation. In the cyclogenesis process, "mixing" of the potential vorticity field also occurs isentropically and the mixing of this field also involves both reversible and irreversible processes. Our focus here will be entirely upon non-isentropic mixing.

4.1. Mixing, stirring, and diffusion

If we are to discuss the diapycnal mixing of initially distinct air masses, we clearly need to have an unambiguous definition of mixing. In this regard, it is essential to distinguish stirring from mixing. Stirring involves an adiabatic redistribution of fluid elements, which is reversible. It is also important to realize that stretching of a material interface does *not* increase the degree of mixing. The deformation and stretching of a material interface, such as that illustrated in Fig.13, can be achieved simply by rearranging the location and the shape of fluid parcels in the system.

The definition of irreversible mixing that we will employ relies on the concept of a "background" or "base" part of the potential energy as in Winters et al. (1995) and CP. The base potential energy (BPE) is the fraction of the total potential energy which cannot be released by any adiabatic rearrangement of fluid parcels. Mathematically, BPE can be defined as the smallest achievable value of the total potential energy that can be reached by any adiabatic redistribution of fluid elements over the entire domain. It is apparent

from the definition that no adiabatic process can change BPE, and thus the development of BPE represents the consequence of irreversible mixing without any contribution from (reversible) "stirring". Therefore, we will refer to the rate of increase of BPE as a "non-isentropic mixing rate" or "irreversible mixing rate"

$$MIX(t) \triangleq \frac{d}{dt} BPE(t). \tag{12}$$

Once the value of BPE is obtained, APE can be calculated as the difference between the total potential energy (TPE) and BPE. The net diffusion ($\mathrm{DIF_N}$) is defined as the domain integral of the energy conversion from internal energy (IE) to TPE. The concepts introduced herein are illustrated schematically in Fig.14. Note that internal energy in the anelastic model does not contribute to the conservation of energy and rather works as a passive reservoir of energy.

The net diffusion is often simply termed "diffusion", and can be expressed for our anelastic model as

$$DIF_N = \Big[DIF\Big] = \frac{g}{\theta_0}\Big[z\,\boldsymbol{\nabla}\bullet(\rho_0\,K_m\boldsymbol{\nabla}\theta)\Big]. \tag{13}$$

In the cases of mixing analyses of shear flows undergoing Kelvin-Helmholtz instability, the net diffusion can be evaluated entirely on the basis of the integral along the top and bottom boundaries and is essentially constant for the following three reasons: (i) both diffusion coefficient and reference-state density are constant and thus the volume integral can be evaluated by surface integrals on the boundaries, (ii) the surface integrals on x boundaries and y boundaries cancel, and (iii) stratification remains unperturbed near the top and bottom boundaries. Therefore, the net diffusion in this case can easily be interpreted as the steady increase of potential energy due to the presence of the background

stratification, whereas the mixing is the enhanced homogenization due to the stretched contours, which in turn is due to the breaking of the K–H billow [1]. Our case is, however, more complex and the net diffusion term changes significantly primarily because strong "action" occurs adjacent to the bottom surface.

4.2. Calculation of base potential energy

A direct method of caluculating BPE was first discussed by Winters et al. (1995) and improved by CP under the Boussinesq approximation. The procedure employed in such analysis has recently been summarised in detail in Peltier and Caulfield (2003). We find that the calculation of BPE remains simple for a generalized anelastic system (GAS), which employs either an isentropic or a non-isentropic reference state. Whereas density, temperature and potential temperature are all conserved for any adiabatic displacement of a fluid element under the Boussinesq approximation, it is only potential temperature θ that is conserved in a GAS. Note also that potential energy in a GAS is estimated by the spatial distribution of potential temperature. Hence, we can employ the potential temperature θ for the index of the sorting part of the rearrangement procedure that is employed to calculate BPE in place of the absolute temperature in the case of the Boussinesq fluid.

The next step required in the determination of BPE is the flattening and layering of the fluid elements. This step is also generalized for a GAS to take into account the compressibility of the fluid. The thickness of each layer must be calculated to satisfy the "modeled" compressibility associated with the approximate conservation of mass which can be stated for a small fluid element of volume δV as

$$\rho_0(z)\ \delta V = \text{const.} \tag{14}$$

This formula is consistent with the approximate continuity equation for anelastic models which is obtained simply by ignoring the first order terms in $\frac{\rho_1}{\rho_0}$.

Therefore, the final state of the fluid after the rearrangement consists of stably stratified thin layers of fluid elements with unequal thickness as illustrated in Fig.15. For the layering of a fluid element, the thickness and the location of the center of mass must be obtained simultaneously. The details of the procedure employed to determine the layered state are described in the Appendix. Once the adiabatic layered state has been achieved, we employ the usual definition of the total potential energy to calculate the potential energy of the rearranged state, namely

$$PE_G(t) \triangleq -\int_V \rho_0(z)\, g\, z\, \frac{\theta_1(\boldsymbol{x},t)}{\theta_0(z)}\, dV. \tag{15}$$

4.3. Evolution of base state potential energy and mixing rate

Evolution of the total and base potential energy is displayed in Fig.16a for Eddy2. The difference between these two curves indicates the available potential energy. The net gain of BPE during the main life cycle (from day 9 to day 17.75) of Eddy2 is only 6% of the loss of the total potential energy. This indicates that the net impact of irreversible mixing is much weaker than reversible stirring. The energy conversions that are effected by the dramatic events that occur during a synoptic-scale baroclinic-wave life cycle are essentially reversible in so far as diapycnal processes are concerned. This conclusion is, of course, subject to the caveat that it depends upon the validity of the assumption that our numerical simulations have adequately represented the impacts of subgrid-scale processes.

The evolution of base potential energy is summarized in Fig.16b and 16c for all cases with different model parameters. The influence of the stratification contrast, S_C, is minor

as shown in Fig.16b. However, it is interesting to note that the increase of BPE is not a monotonic function of the stratification contrast. At day 18, for example, the BPE is smallest when $S_C = 6$ followed by cases with $S_C = 4$, $S_C = 3$, and $S_C = 9$. Note that we have introduced a new run with $S_C = 4$, to more fully test the monotonicity of mixing effects against the stratification contrast.

On the contrary, the strong influence of the assumed level of small-scale turbulence is evident in Fig.16c. The evolution for the case labeled Control clearly shows the impact of the implicit diffusivity due to the discrete numerics of the model, and the rapid mixing during the saturation and decay stages is evident from day 13 to day 17. In this sense, the evolution is very similar to the other cases with explicit parameterization of turbulence except that the mixing is much weaker.

The evolution of the mixing rate, $MIX = \frac{d}{dt}BPE$, is summarized in Fig.17. The maximum mixing rate reaches 22 μW m^{-3} for case Eddy2, which is achieved at day 15.5 during the early decay stage of the life cycle. This magnitude is only 4% of the maximum magnitude of the reversible stirring rate (i.e., VHS). Nevertheless, the evolution of irreversible non-isentropic mixing and its dependence on the assumed strength of the turbulence is clearly quantified.

It is also of interest for us to identify the spatial distribution of strong mixing activity. In the cases of mixing analyses of K-H instability, both Winters et al. and CP have demonstrated that the examination of the adiabatically rearranged (i.e., "sorted") profiles of the potential temperature is useful to identify the active region of mixing.

Displayed in Fig.18a are examples of such sorted profiles of potential temperature before and after the single life cycle event of Eddy2. It is apparent that the irreversible (non-

isentropic) mixing due to the baroclinic life cycle only has a minor smoothing effect even for the case with strongest viscosity. The exception, that can be identified in Fig.18b, might be the cooling of an air mass ($285 < \theta < 295$ K), which was initially located in the band that extends from the frontal region to the upper troposphere on the north side of the jet, and warming of the colder air. Although not conclusive, this seems to indicate that the most active mixing takes place along the surface front, which is consistent with the morphological features that we have identified in the conventional analysis in Section 3. Further investigation of the spatial distribution of mixing will be provided in the next section using an alternative measure.

5. Entropy-based mixing diagnosis

In this section, the concept of thermal entropy and a novel measure of irreversible mixing is discussed. Following the description of these quantities, the entropy-based diagnosis is applied to the simulated life cycles.

5.1. Thermal entropy and an irreversible activity index

Entropy helps to describe the development of an irreversible mixing process because it is the direct measure of irreversible processes in general. Unfortunately, a realistic general definition of entropy is beyond the scope of traditional thermodynamics and is still under discussion for a fluid element in motion because it is not in an equilibrium state (e.g., Jou et al., 1996). However, we may simply define a part of the entropy which is purely due to the thermodynamic state of a fluid element by assuming a local thermal balance or, most importantly in this context, by ignoring the presence of motion. We employ this quantity and call it "thermal entropy" or simply entropy in this paper. On the assumption

that the contribution of strongly non-equilibrium effects is small for synoptic-scale and meso-scale motion of the atmosphere, the entropy is expected to be a useful measure of the development of irreversible processes including mixing.

For example, it is well-known (e.g. Gill, 1982) that the specific entropy of an ideal gas in an equilibrium state can be defined as

$$s \triangleq c_p \log\theta + \text{constant}. \tag{16}$$

We may set the arbitrary constant to zero for our application as our interest is in the change of entropy. This is eqivalent to setting the arbitrary reference temperature to 1 K. We employ this definition as the definition of the specific "thermal entropy".

In the anelastic approximation, the definition of specific entropy in (16) is not affected. However, the equation of mass conservation is approximated as (14). Therefore, the density in the definition of the entropy of a fluid element should be replaced by the reference density. This defines an entropy which is precisely conserved for an adiabatic process under the anelastic approximation. Using this definition, we can estimate the total entropy in the whole domain in terms of the entropy per unit volume as

$$S_T(t) \triangleq \Big[\rho_0\, s\Big]. \tag{17}$$

Unlike the base potential energy, which was employed in the previous section, entropy is defined locally. Therefore, we may reasonably estimate the spatial distribution of the strength of irreversible (non-isentropic) activity by using the Lagrangian time derivative of the thermal entropy. For an anelastic system, the "irreversible activity index" is thus defined as

$$I_{IA} \triangleq \rho_0 \frac{\mathrm{D}\, s}{\mathrm{D}\, t} = \rho_0\, c_p \frac{\mathrm{D}}{\mathrm{D}\, t} \log\theta. \tag{18}$$

The development and the spatial distribution of the irreversible activity index will tell us quantitatively when and where irreversible processes are taking place.

Note that, in the anelastic approximation, the buoyancy is measured in terms of the normalized potential temperature anomaly and thus the thermal entropy defined above may also be interpreted as a measure of buoyancy. In fact, the irreversible activity index defined here is proportional to the time derivative of buoyancy in the classical anelastic approximation, namely

$$I_{IA} \approx \rho_0 \, c_p \frac{1}{\theta_0} \frac{\mathrm{D}\,\theta}{\mathrm{D}\,t} \propto \frac{\mathrm{D}}{\mathrm{D}\,t} \left(\frac{\theta}{\theta_0} g \right). \tag{19}$$

Moreover, we may also derive a measure of irreversible activity in terms of (the rate of the change of) energy. Since such energy-based analyses are more conventional than those based upon entropy, it might be more useful to employ the *diagnostic* heating rate (per unit volume) that is defined as

$$H_D \stackrel{\triangle}{=} \rho_0 \, T \frac{\mathrm{D}\,s}{\mathrm{D}\,t} \approx \frac{c_p \rho_0 T_0}{\theta_0} \frac{\mathrm{D}\,\theta}{\mathrm{D}\,t}, \tag{20}$$

for a generalized anelastic fluid model. Note that this quantity is precisely the conventional diabatic heating rate and that diabatic heating is always associated with irreversibility. However, the magnitude of the irreversible activity captured in this way also includes that due to implicit numerical diffusivity. This representation is therefore especially useful for diagnosis.

5.2. Evolution of entropy and base potential energy

The evolution of spatially integrated entropy is summarized in Fig.19 for all cases with different model parameters, together with that of base potential energy (BPE). The important feature in both panels of Fig.19 is the very good correlation between the increase

of BPE and that of the thermal entropy. In fact, the evolution of these two quantities are almost identical when initial biases are removed and the latter is multiplied by a characteristic temperature, T_*, that is empirically obtained for each case. We will not attach any particular physical meaning to this characteristic temperature, but simply note that a monotonic decrease of the characteristic temperature accompanies the increase of the stratification of the stratosphere as stated in the key of Fig.19b. Note especially that a common characteristic temperature is employed in Fig.19a for all cases of Control, Eddy1, and Eddy2, which are initialized with the same potential temperature field.

5.3. Vertical structure of irreversible activity

We may next proceed to distinguish the mixing along the tropopause from that which occurs along the surface fronts. Because the mixing rate in Section 4 was defined as a scalar characteristic of the entire system, the analysis of the spatial localization of the irreversible mixing was not very successful. Fortunately, however, the analysis in Section 5.2 demonstrated a strong correlation between the increase of base potential energy and that of domain-integrated thermal entropy. Therefore, the irreversible activity index, discussed in Section 5.1, can be employed to diagnose the spatial structure of irreversible mixing activity.

The irreversible activity index was calculated from data sets saved every three hours. In order to ensure that the numerical estimation of the Lagrangian time derivative is accurate, it was explicitly confirmed that the domain integral of the irreversible activity index is equal to the time derivative of the domain integral of thermal entropy. This is particularly important from the computational point of view because the Lagrangian time derivative of a primarily conservative quantity, such as potential temperature, is the small

difference between local time derivative and advection. The advection was evaluated using the two-point average second-order centered difference scheme, namely

$$u\frac{\partial s}{\partial x} = \frac{1}{2}\left(u_{i-\frac{1}{2}}\frac{s_i - s_{i-1}}{DX} + u_{i+\frac{1}{2}}\frac{s_{i+1} - s_i}{DX}\right), \tag{21}$$

for the x component.

The vertical structure of the activity was obtained as a horizontal average and is summarized in Fig.20. The profile shown is the temporal average from day 15 to day 16. For all cases, there exists a dominant peak of positive activity at the bottom surface below a region of negative activity and broad regions of weakly positive and negative activity underneath the tropopause. Note that a region of active mixing is displayed as two adjacent regions of positive and negative irreversible activity in this figure because the heat transfer associated with mixing involves both heating and cooling in the adjacent regions. As expected, the increase of turbulent diffusivity resulted in the increase of irreversible activity both near the surface and in the vicinity of the tropopause folds. There is also a small peak near $z = 12$ km though it is hardly noticeable except in the result from Eddy2.

Further details of the spatial structure are shown in Fig.21 as the zonal mean of the mixing activity index from Eddy2. The mixing near the tropopause folds is quantified and visualized as well as the strong mixing near the surface (contours of high values, which only exist below 2 km in height, are omitted). Also interesting is the clear evidence of the existence of small regions of active mixing away from the two major regions of mixing. The most notable example exists above the tropopause near (y, z) = (3000 km, 12 km), which corresponds with the very small peak in Fig.20.

6. Conclusions

Synoptic-scale baroclinic wave life cycles along the mid-latitude jet stream were simulated by employing a non-geostrophic non-hydrostatic model, and the evolution was analyzed in detail. "No-noise" initialization of well-balanced initial flow allows us to clearly identify the distinctive period of normal mode growth as well as the presence of an impulse of positive barotropic energy conversion during the saturation stage of the growth of eddy kinetic energy. We have confirmed that the seclusion is initiated by a localized breakdown (or "rupture") of the surface front, which triggers the ensuing development of a deep, horizontally localized, vortical disturbance that reaches the tropopause. This event terminates the negative barotropic energy conversion in the vicinity of the northern extrema of the front, and causes an apparent positive impulse of barotoropic energy conversion in the domain-integrated energetics.

It is also useful to note that the frontal rupture takes place prior to the onset of the viscous inhibition of frontal collapse. Although frontal collapse at the rupture point is prevented by diffusion, the temperature gradient along the warm and cold front continues increasing even after the event except for the location of the rupture.

By comparing a series of simulations initialized with different degrees of stratification contrast between stratosphere and troposphere, the amplitude of the "synoptic-scale deformation" of the tropopause was found to be strongly sensitive to the stratification contrast, as one might expect. Although the influence of the increased contrast from the realistic level assumed in Control was minor, a large amplitude deformation was observed when the stratification contrast was reduced to 3 from the climatological value of 6. However, the behaviour of the descending "tongue" of air that constitutes the tropopause fold was

found to be practically insensitive to the change of the stratification contrast as if the folds were induced solely by some tropospheric mechanism.

The assumed strength of the grid-scale turbulence, that is represented in the model using a first order closure with a Richardson number dependent mixing coefficient, was shown to have little influence on the deformation of the tropopause, although it significantly altered the meso-scale structure near the surface. The smoothing effect of the momentum diffusion was clearly recognized in the lower troposphere after the decay stage of eddy kinetic energy, but the influence was minor in the vicinity of the tropopause according to our examination of the PV structure.

The degree of irreversible (non-isentropic) mixing in the nonlinear life-cycles has been evaluated by directly examining the evolution of the base potential energy. Despite the strong deformation of the tropopause, our mixing analysis showed that the baroclinic wave life cycle is essentially reversible in the sense that the irreversible change of potential energy is almost negligible compared with the reversible change of potential energy due to the baroclinic stirring. In so far as irreversible mixing is concerned, the stratification contrast had a minor non-monotonic influence on these flows. On the other hand, the intensity of the irreversible mixing was found to be very sensitive to the assumed intensity of turbulent diffusion, as expected. However, the change of potential energy through irreversible mixing was found to be only a few percent of that due to reversible stirring for all cases.

We have also introduced an alternative entropy-based measure of mixing. It was explicitly demonstrated that the evolution of entropy is virtually identical to that of the base potential energy and we confirmed that the mixing activity was most intense along the surface fronts, followed by the vicinity of the deformed tropopause.

One "ingredient" which is missing in the present model is the contribution of strong gravity waves such as those induced by topography, nonuniform heating of the surface, or diabatic heating due to moist convection. Our simulations were "gently" initialized by extremely weak noise and thus generation of gravity waves by the initial shock is also practically nonexistent. Also missing is the bottom boundary layer, which could significantly alter the mixing rate near the surface. As a further step in this series of investigations, we plan in future work to diagnose the occurrence of meso-scale shear instabilities using models with higher numerical resolution.

Appendix A: Layering of fluid elements required to calculate base potential energy

This appendix describes the procedural details of the adiabatic "layering" of fluid elements that is required for the purpose of the calculation of the base potential energy discussed in Section 4. As we will see below, the conservation of mass constraint requires careful solution of a quadratic equation to determine the new center of mass for each fluid element.

Firstly, we need to ensure that mass is conserved for the entire system as well as for each fluid element. We thus assume that the density profile after the layering of fluid elements is the same as that before the adiabatic rearrangement procedure in the discretized sense. The original density profile of the reference state before the rearrangement procedure is numerically represented by a piecewise-linear function of height with equal intervals for the vertical number of grid-boxes (58 for our analysis). On the other hand, the final profile of the reference state density might be represented, in principle, as an unevenly-spaced piecewise-linear function of height for the total number of fluid elements (i.e., the total

number of grid-boxes of $64\times126\times58 = 467712$). However, if we employed the latter profile, the simultaneous conservation of the total mass and the volume of the fluid domain might be difficult. For example, if we were to calculate the new center of mass as we layer a new fluid element using the analytic expression of the reference-state density, the top height of the entire "layer-cake" might not match the height of the model domain due to the error associated with the difference in the vertical discretization. Therefore, we assume that the reference density profile after the rearrangement is represented by the coarse profile before the rearrangement. In other words, the model domain is assumed to consist of a fixed set of "density layers", within which the density profile is described by a linear function of height. This guarantees the conservation of total mass as the integrated height of the entire "layer-cake" is conserved. In our implementation, the integrated height was conserved to an accuracy of better than 11 digits.

The actual layering is done from the bottom of the domain, beginning with the fluid element with the smallest potential temperature. Since the density profile is prescribed as a piecewise-linear function of height, the first step in the construction of the layered state is to see if there is enough room in the lowermost "density layer", to store the whole fluid element of interest. When the mass of the fluid element of interest is larger than the mass of the "available" (i.e., vacant) portion of the density layer, the element will not fit in the layer. Thus, in this case, the available room is first filled with a portion of the fluid element and the mass of the rest of the fluid element (leftover) is calculated to occupy the bottom portion of the next density layer, which is located just above. The same procedure is repeated until it is certain that the residual mass is smaller than the mass of the next density layer.

When the mass, m_E, of the entire fluid element (or the residual fluid element) is smaller than the mass of the "available" portion of the next density layer, the density profile can be written as a linear function of height as

$$\rho_0(z) = a_L z + \rho_0(z_0), \tag{A1}$$

where a_L is a constant that depends on the density layer. Thus, the mass of a new layer of fluid with thickness, h, can easily be calculated as

$$m_L(z_b, h) = NX\, NY \int_{z0}^{z0+h} \rho_0(z)\, dz, \tag{A2}$$

where z_b represent the height of the bottom of the density layer and the mass is scaled by the horizontal area of one fluid element before the rearrangement. Due to the conservation of mass ($m_E = m_L$), the new layer thickness, h, is determined by solution of the following quadratic equation

$$\frac{1}{2} a_L h^2 + \rho_0(z_b)\, h - \frac{m_E}{NX\, NY} = 0. \tag{A3}$$

We solved this quadratic equation numerically, employing a sixth order Taylor expansion formulation of the analytical solution when it is necessary to avoid a numerical underflow.

Acknowledgments. This research was carried out in the context of the Ph.D programme of Y. H. Yamazaki, which has been supported by Government of Canada Awards to promote scientific collaborations between Canada and Japan. Additional support has been provided through research grant A9627 to W. R. Peltier from the Natural Sciences and Engineering Research Council of Canada. We also appreciate a number of useful comments by Professor Noboru Nakamura on an early version of this manuscript.

Notes

1. The definition of pure mixing in CP is different from the definition of mixing employed by Winters et al. (1995) and present study. CP simply subtracted the constant net diffusion from their definition of "instantaneous mixing rate" because the net diffusion was constant.

References

Boussinesq, J., *Theorie analytique de Chaleur, 2,* Paris, Gauthier-Villars, 1903.

Bush, A. B. G. and W. R. Peltier, Tropopause folds and synoptic-scale baroclinic wave life cycles, *J. Atmos. Sci., 51,* 1581–1604, 1994.

Caulfield, C. P. and W. R. Peltier The anatomy of the mixing transition in homogeneous and stratified free shear layers. *J. Fluid Mech., 413,* 1–47, 2000.

Charney, J. G. The dynamics of long waves in a baroclinic westerly current. *J. Meteorol., 4,* 135–162, 1947.

Clark, T. L., A small-scale dynamic model using a terrain-following coordinate transformation, *J. Comp. Phys., 24*, 186–215, 1977.

Danielsen, E. F. and R. S. Hipskind Stratospheric-tropospheric exchange at polar latitudes in summer, *J. Geophys. Res., 85,* 393–400, 1980.

Eady, E. T. Long waves and cyclone waves., *Tellus, 1,* 33–52, 1949.

Gill, A. E. *Atmosphere-Ocean Dynamics*, 662pp., Academic Press, San Diego, California, 1982.

Hoskins, B. J., M. E. McIntyre, and R. W. Robertson On the use and significance of isentropic potential vorticity maps, *Q. J. R. Meteorol. Soc., 111*, 877–946, 1985.

Lilly, D. K. On the numerical simulation of buoyant convection, *Tellus, 14,* 148–172, 1962.

Lorenz, E. N. Available potential energy and the maintenance of the general circulation, *Tellus, 7,* 157–167, 1955.

Margules, M. Über die energie der Stürme. *Jahrb. kais.-kön. Zent. fur Met.*, Vienna, 1903.

Methven, J. Spirals in potential vorticity. Part II: stability, *J. Atmos. Sci., 55,* 2067–2079, 1998.

Methven, J. and B. J. Hoskins Spirals in potential vorticity. Part I: Measures of structure, *J. Atmos. Sci., 55,* 2053–2066, 1998.

Nakamura, N. Two-dimensional mixing, edge formation, and permeability diagnosed in an area coordinate, *J. Atmos. Sci., 53,* 1524–1537, 1996.

Neiman, J. P., M. A. Shapiro and L. S. Fedor, The life cycle of an extratropocal marine cyclone. Part II: Mesoscale structure and diagnostics, *Mon. Weather Rev., 121,* 2177–2199, 1993.

Peltier, W. R. and C. P. Caulfield, Mixing efficiency in stratified shear flows., *Ann. Rev. Fluid Mech., 35,* 135–167, 2003.

Polavarapu, S. M. and W. R. Peltier, The structure and nonlinear evolution of synoptic-scale cyclones: Life-cycle simulations with a cloud-scale model. *J. Atmos. Sci., 47,* 2645–2672, 1990.

Shapiro, M. A. and D. Keyser, Fronts, jet streams, and tropopause, *Extratropical Cyclones*, The Erik Palmèn Volume, C. W. Newton and E. Holopainen Eds, Amer. Meteorol. Soc., 167–191,1990.

Winters, K. B., P. N. Lombard, J. J. Riley, and E. A. D'Asaro, Available potential energy and mixing in density-stratified fluids, *J. Fluid Mech., 289,* 115–128, 1995.

Yamazaki, Y. H. and W. R. Peltier, The existence of subsynoptic-scale baroclinic instability and the nonlinear evolution of shallow disturbances, *J. Atmos. Sci., 58,* 657–683, 2001.

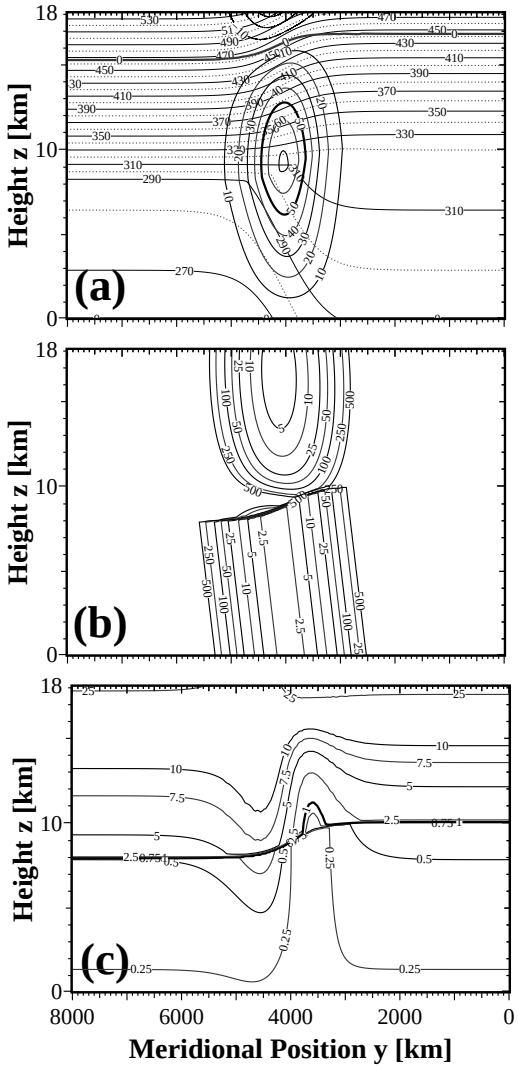

Figure 1. The initial fields for the control run: (a) Potential temperature (thin lines) and zonal wind (thick lines). (b) Richardson number. The contour levels are 2.5, 5, 10, 25, 50, 100, 250, and 500. (c) The potential vorticity. The contour levels are 0.25, 0.5, 0.75, 1.0 (thik line), 2.5, 5.0, 7.5, 10, and 25 PVU (1 PVU = 10^{-6} K m^2 kg^{-1} s^{-1}). The value of PV is positive in the entire domain.

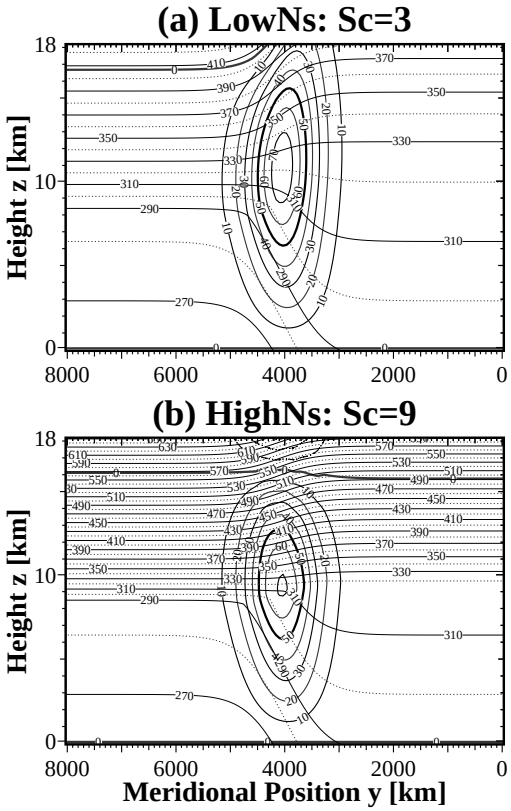

Figure 2. The initial fields for (a) LowNs and (b) HighNs. The notation and the contour intervals are the same as Figure 1a.

Table 1. Summary of simulation conditions

Run	K_c [m^2 s^{-1}]	$N_S{}^2$ [s^{-4}]
Control	0	6×10^{-4}
LowNs	____	3×10^{-4}
HighNs	____	9×10^{-4}
RigidLid	____	∞
Eddy1	10^2	____
Eddy2	10^3	____

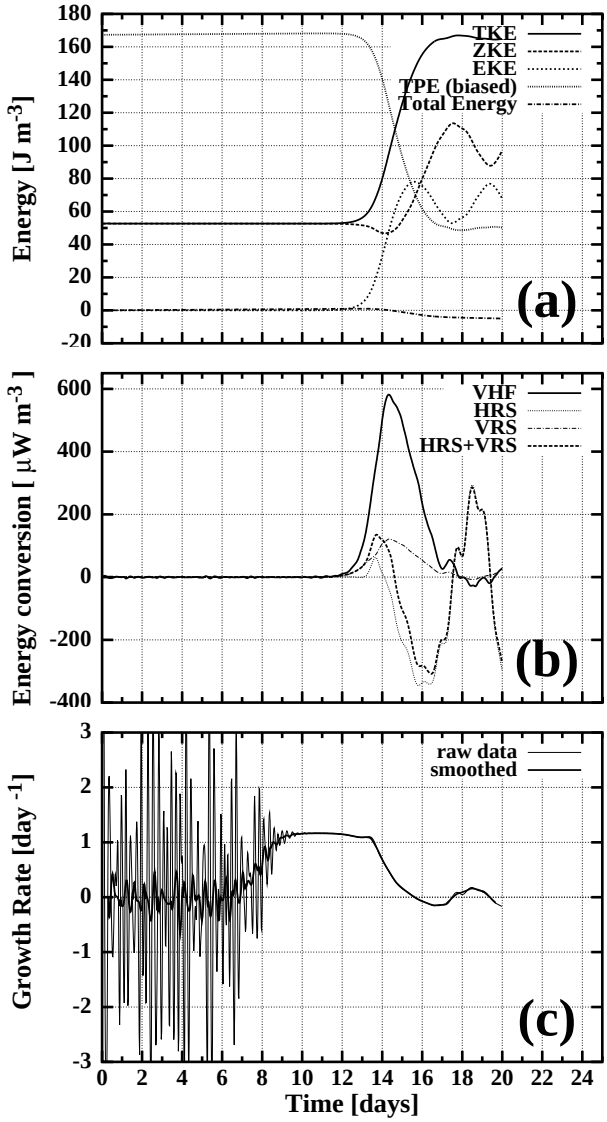

Figure 3. Evolution of energetics for case Control: The energetics is represented by evolutions of (a) energy components, (b) energy conversion terms, and (c) growth rate. The smoothed curve in the growth rate evolution is obtained as a weighted running mean.

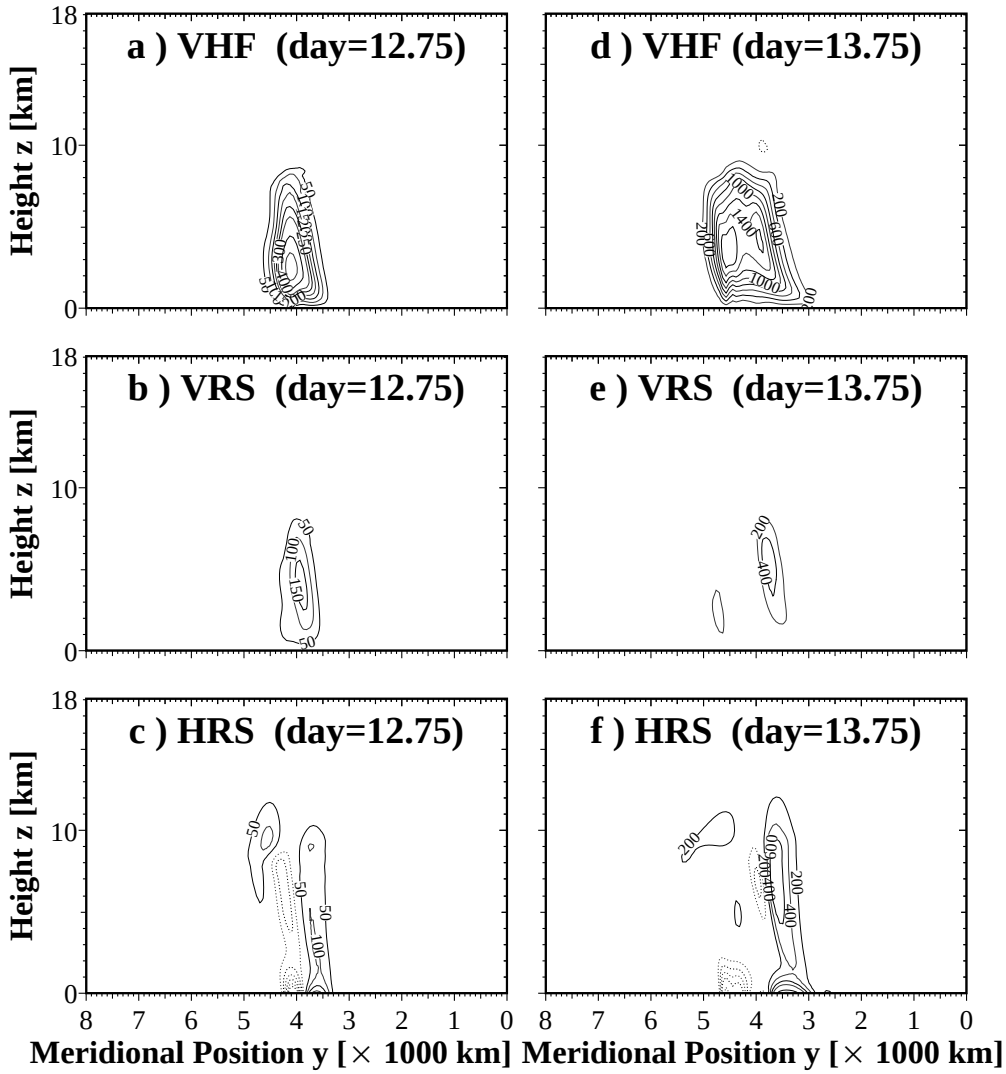

Figure 4. Spatial structure of energy conversion terms from the Control run: The energy conversion from the mean flow to the 4000 km wave component are shown in μ W m^{-3} for Vertical Heat Flux (top), Vertical Reynolds Stress (middle), and Horizontal Reynolds Stress (bottom). The left panels shows results at day 12.75 while the right panels are obtained at day 13.75. Contour intervals are 50 μ W m^{-3} for (a)–(c) and 200 μ W m^{-3} (d)–(f).

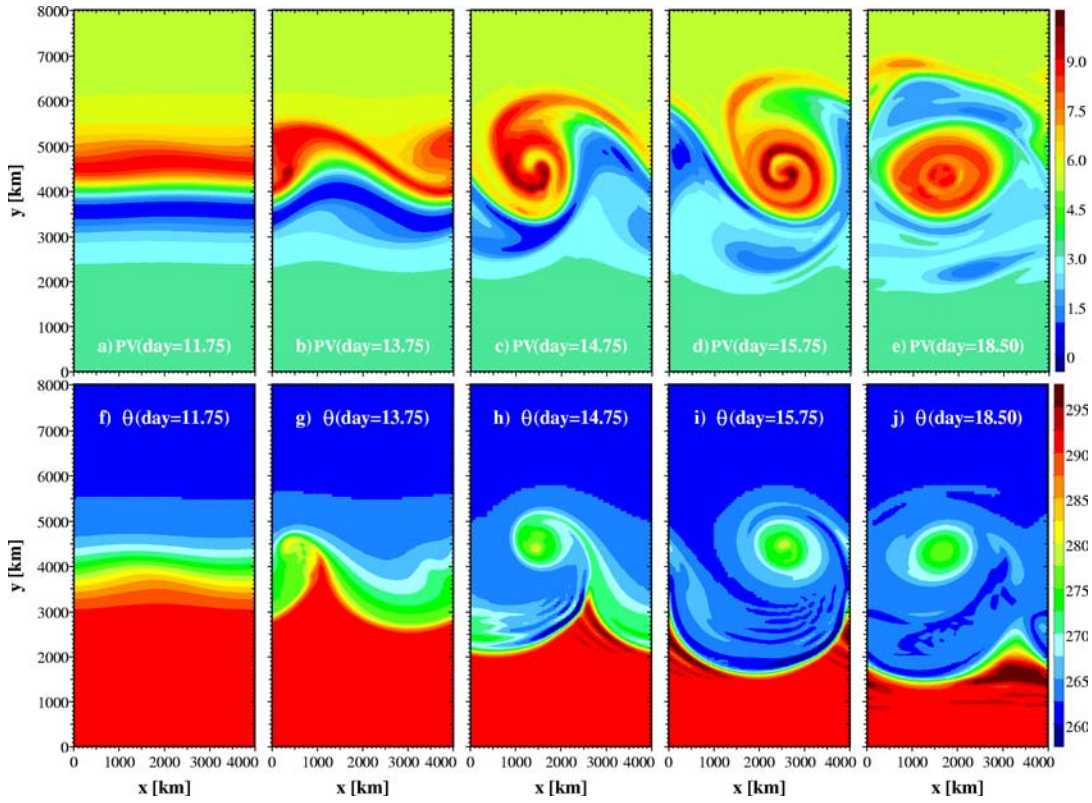

Figure 5. Upper and surface cyclogenesis from Control: Successive planform snapshots of (a)–(e) potential vorticity on $\theta = 325$ K isosurface and (f)–(j) surface potential temperature.

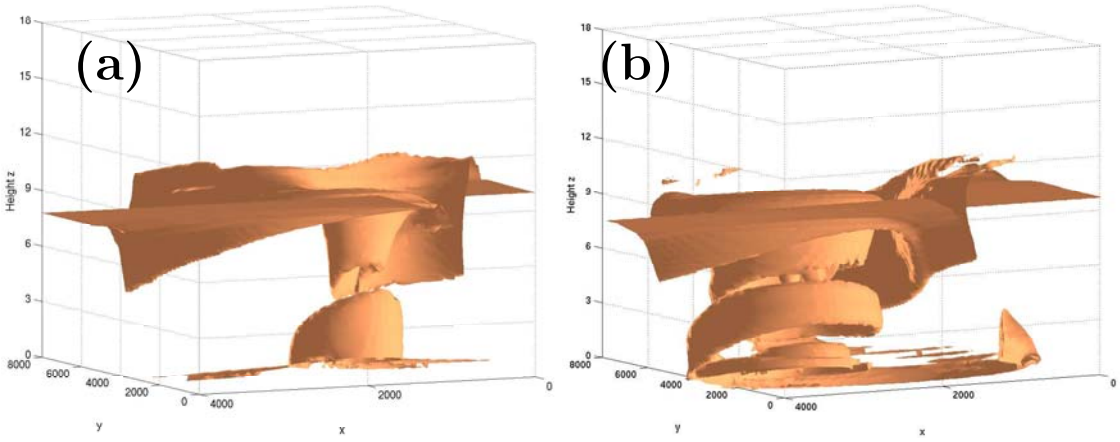

Figure 6. A three-dimensional deformation of tropopause: The isosurface of PV = 1 PVU from Control is rendered at model time (a) 14.25 and (b) 15.75 days. The view point is northwest of the simulation domain for the eastward mean flow.

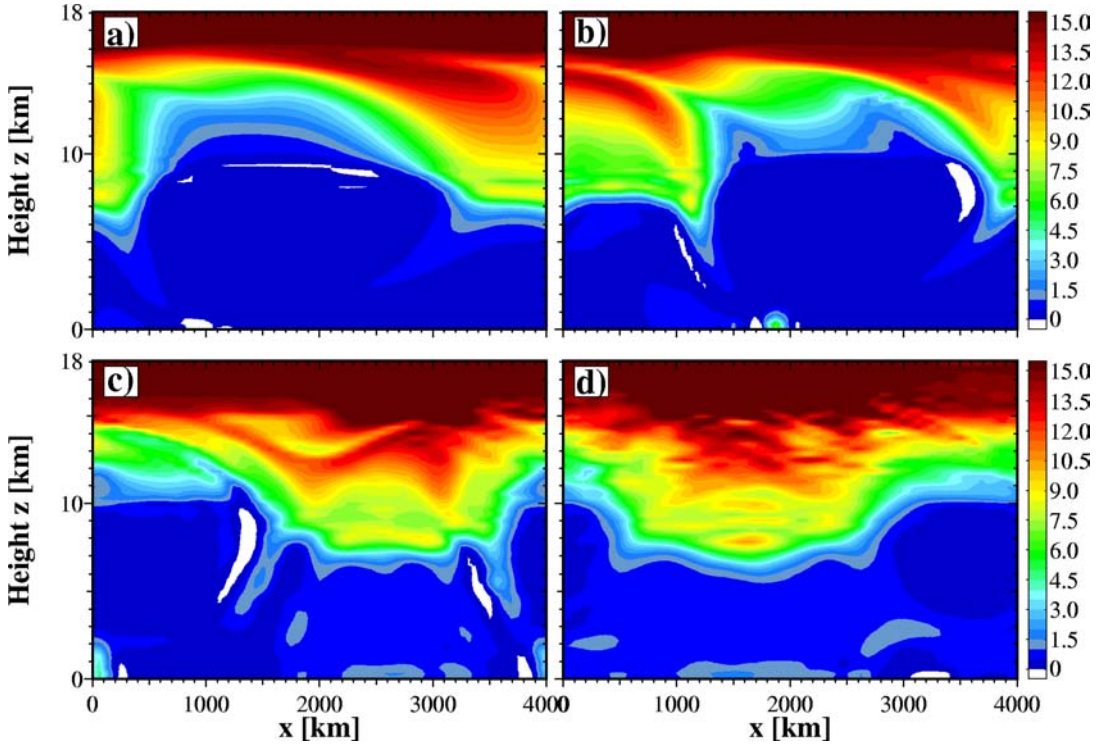

Figure 7. Evolution of the vertical PV structure along $y = 4000$ km for the case Control: The times are (a) 13.75, (b) 14.25, (c) 15.75, and (d) 18.5 days.

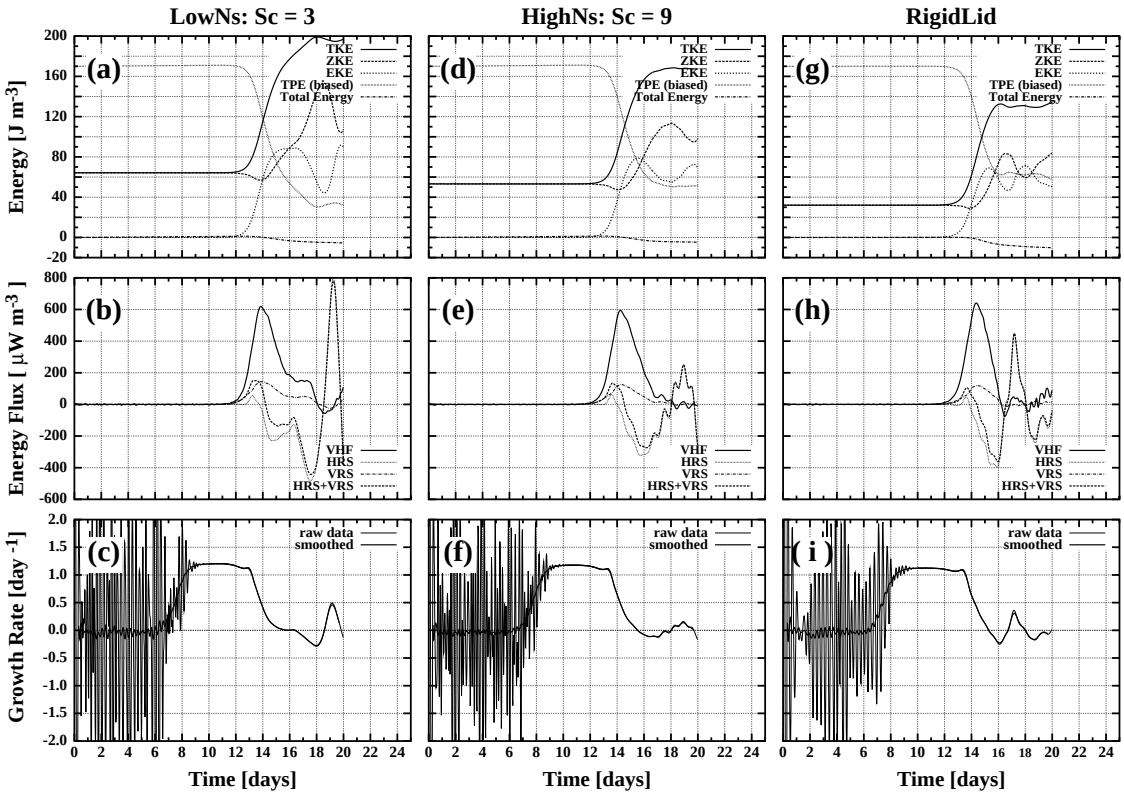

Figure 8. Energetics of cases LowNs (left panels), HighNs (center), and RigidLid (right). The same notations are employed as in Figure 3 for each column.

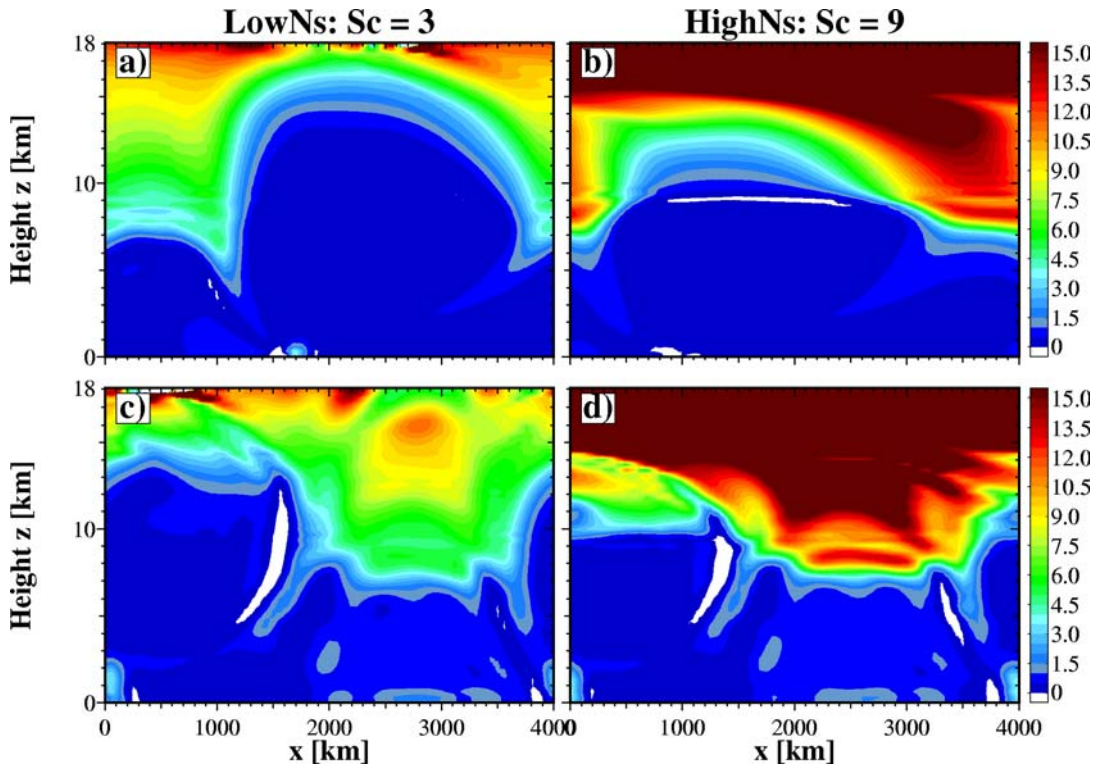

Figure 9. The vertical PV structure along $y = 4000$ km for cases LowNs (left) and HighNs (right): Upper panels indicate the PV structure when the amplitude of the synoptic-scale deformation of the tropopause is largest, namely at model time 13.675 days for both (a) and (b). Lower panels show the PV structure when the tropopause fold reaches maximum descent, namely at model time (c) 15.125 days and (d) 15.675 days.

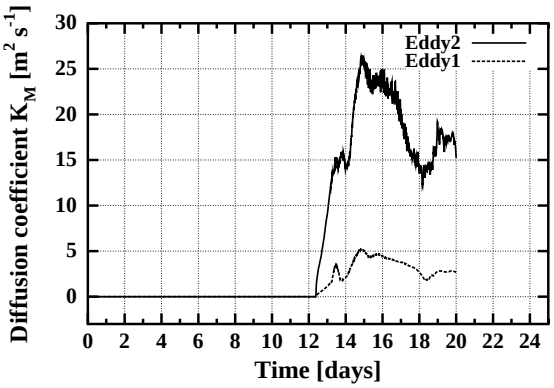

Figure 10. Evolution of the spatial maximum of turbulent viscosity.

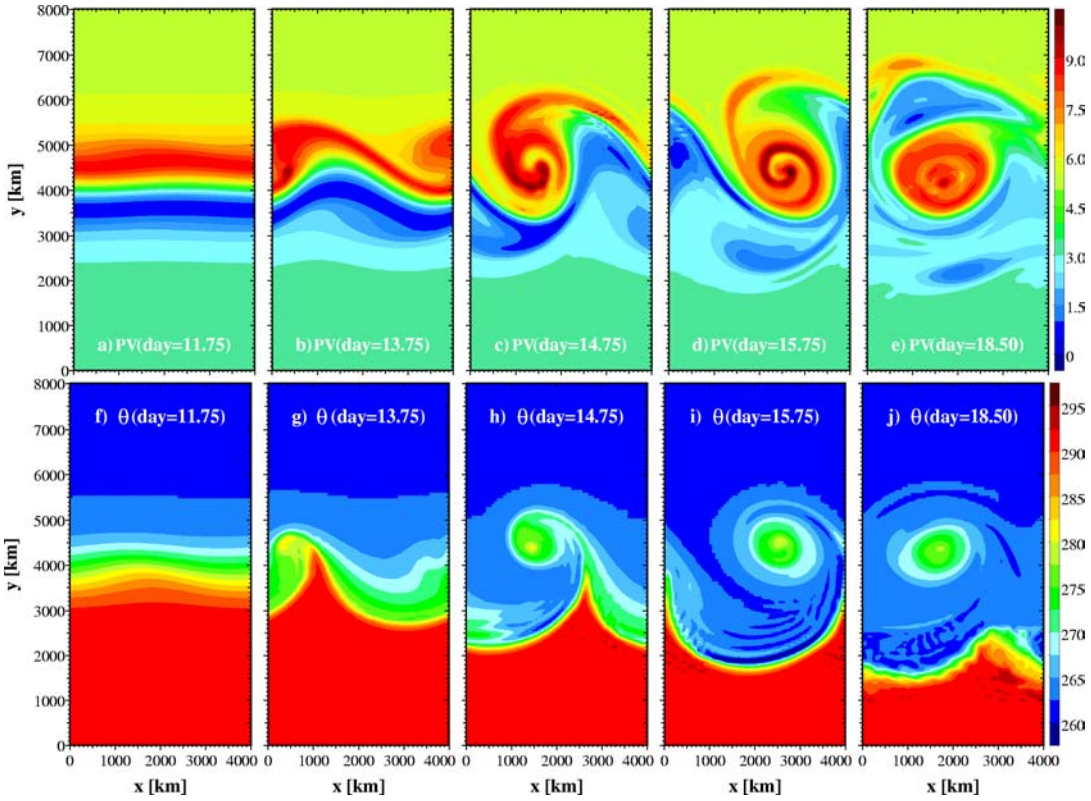

Figure 11. Evolution of upper and surface cyclogenesis for the case Eddy2. The same convention is employed as Figure 5.

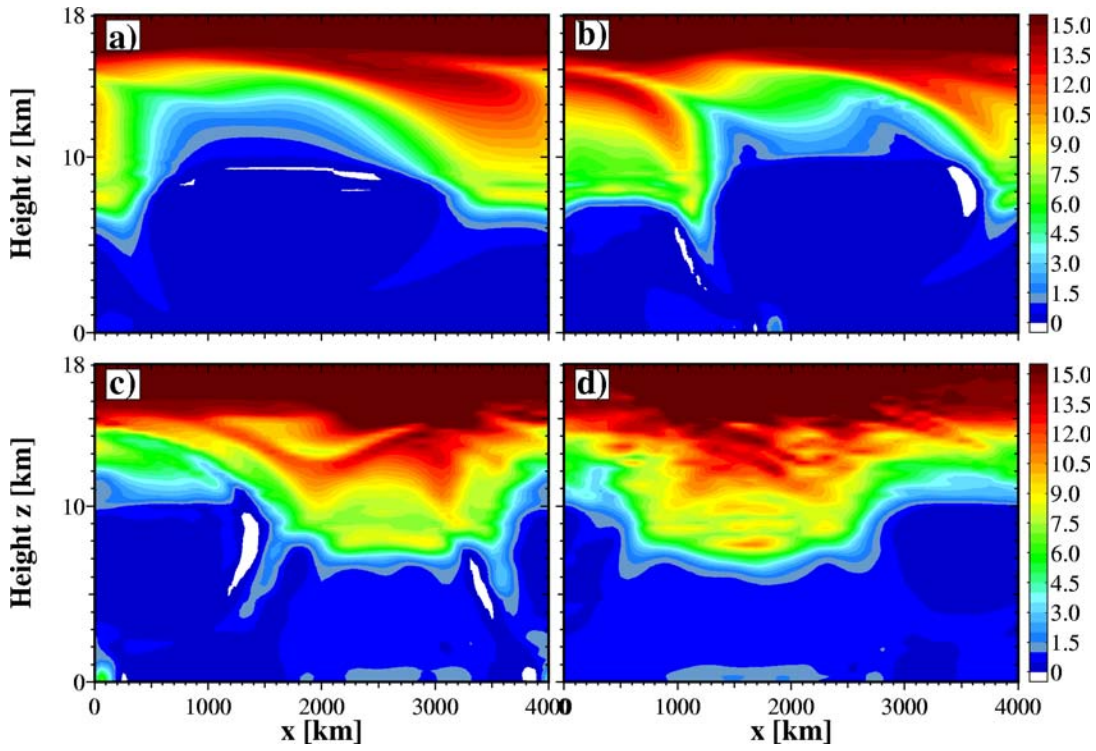

Figure 12. Evolution of the vertical PV structure along $y = 4000$ km for the case Eddy2: The same notations are employed as in Figure 7.

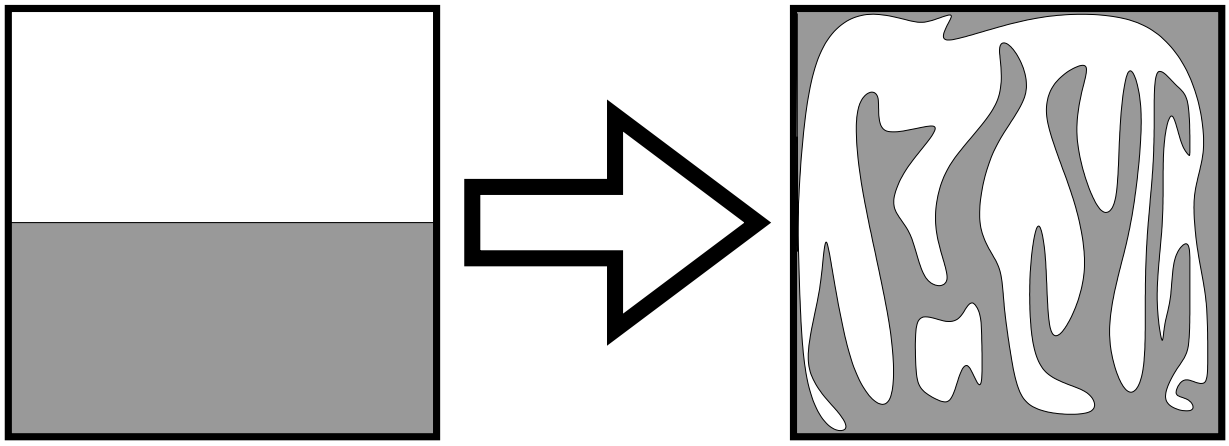

Figure 13. Deformation of material interface due to relocation of fluid elements

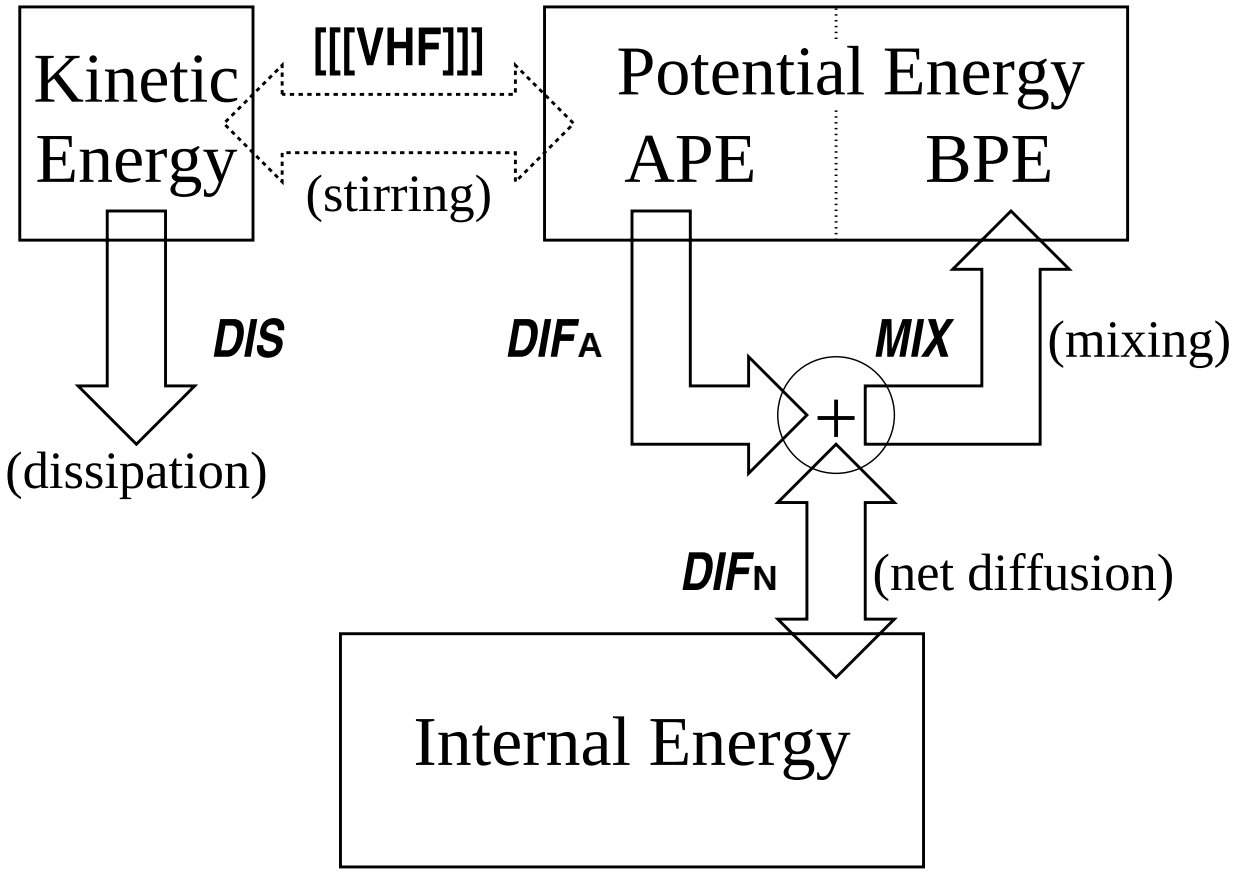

Figure 14. Component energy and energy conversion: Solid and dashed arrows represent irreversible and reversible conversion of energy respectively, and a head of arrow indicates a possible direction of energy conversion.

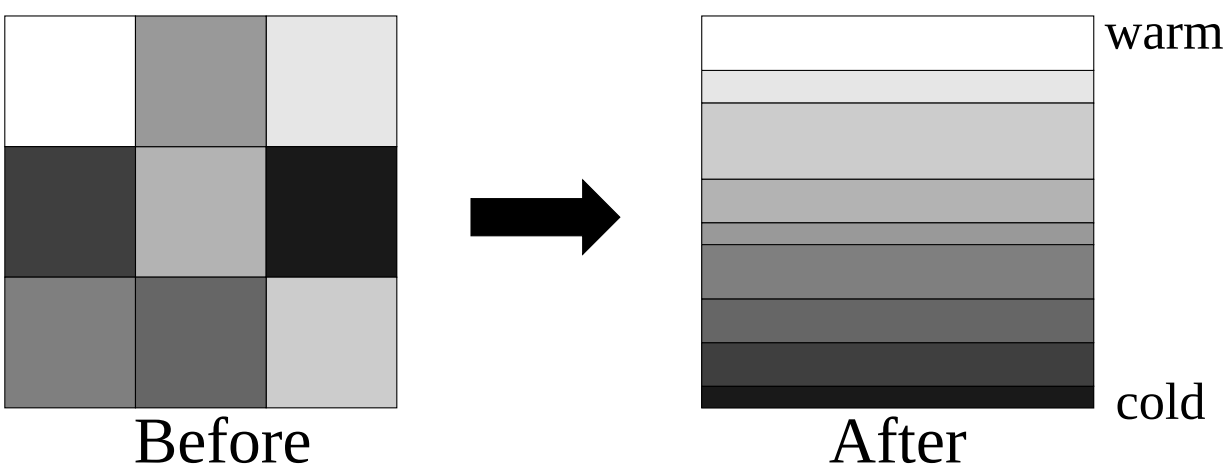

Figure 15. Adiabatic relocation of fluid elements in the anelastic model.

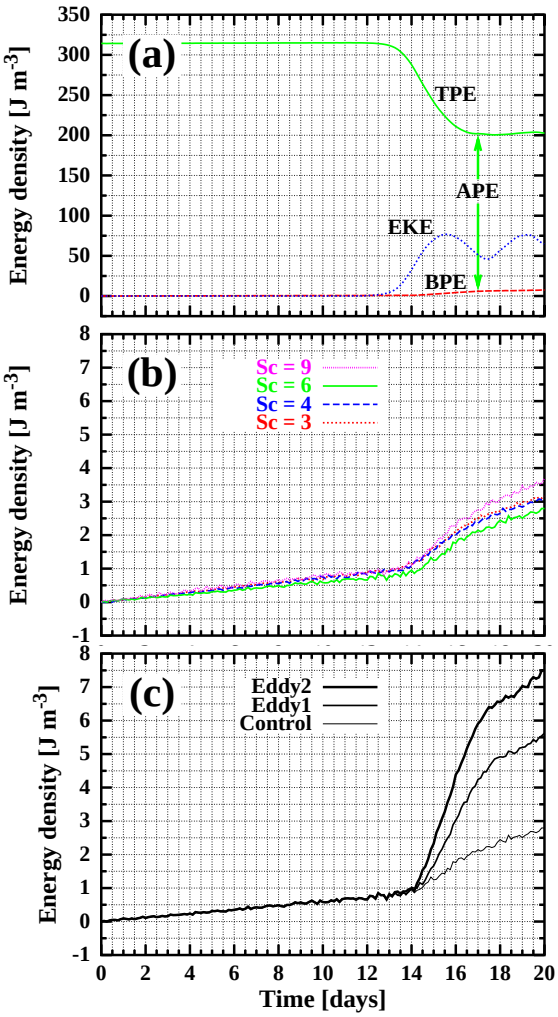

Figure 16. Evolution of base potential energy: (a) Comparison of total and base potential energy and eddy kinetic energy from Eddy2. Available potential energy is indicated as the difference between total and base potential energy. (b) Sensitivity of BPE to stratification contrast. (c) Sensitivity of BPE to turbulence diffusivity.

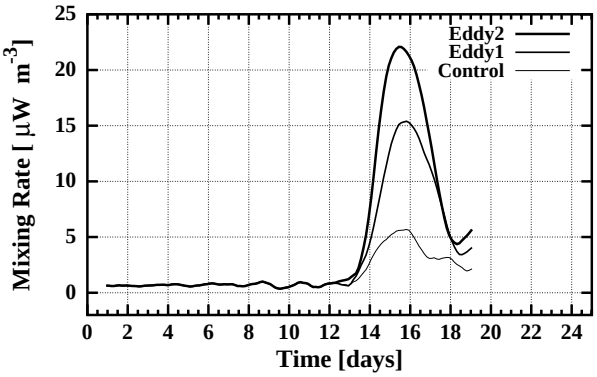

Figure 17. The evolution of irreversible mixing rate and its sensitivity to the assumed strength of turbulent diffusion. The curves have been smoothed by a weighted running average with characteristic time of 2 days.

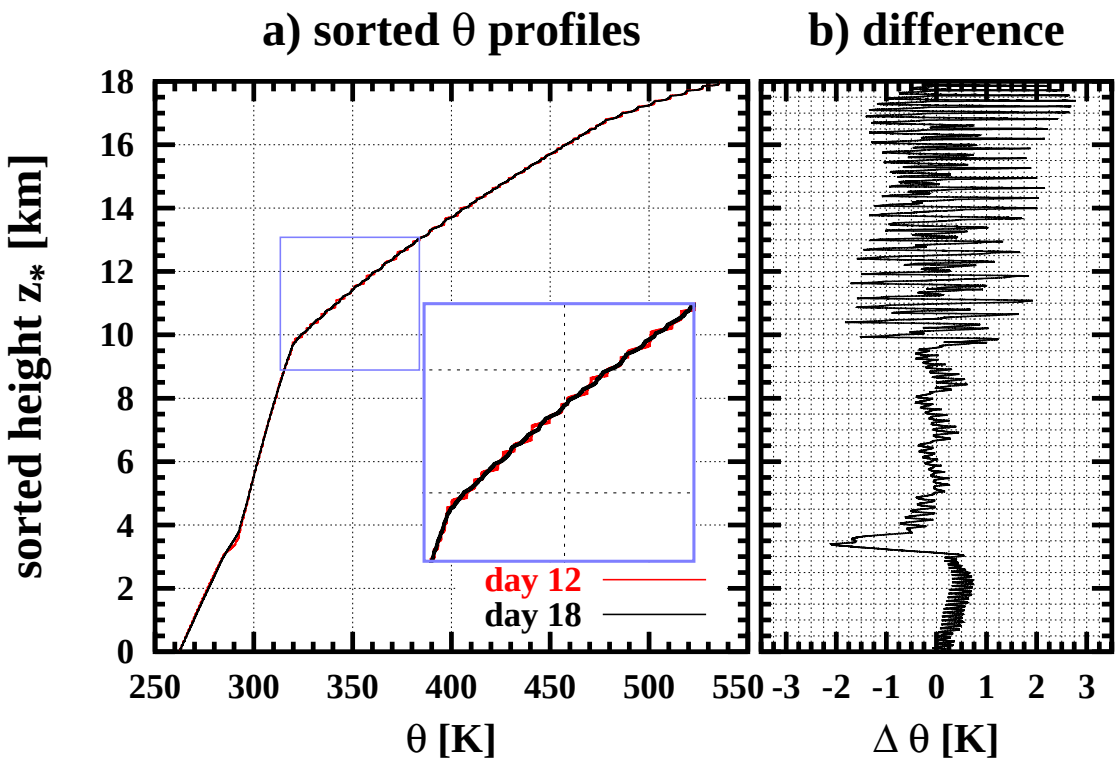

Figure 18. The potential temperature after adiabatic rearrangement: (a) The sorted profiles obtained at model day 12 and day 18 of Eddy2. A close-up subfigure of the bounded region is inlayed. (b) Difference of the sorted potential temperature profiles.

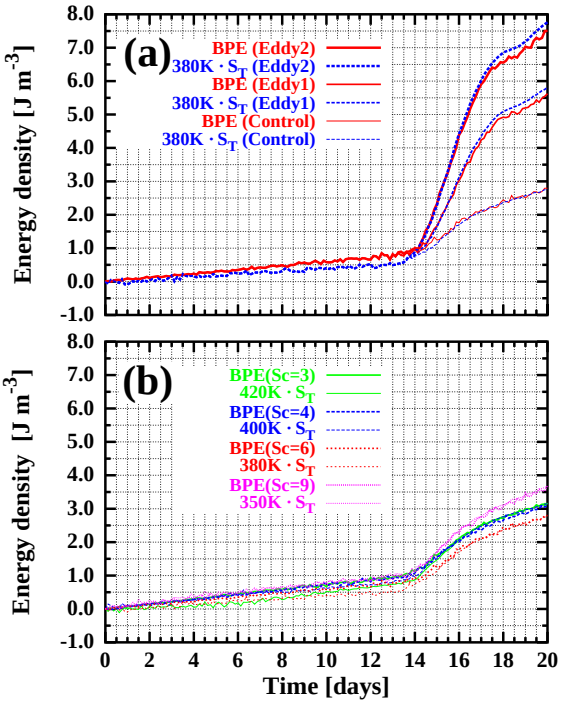

Figure 19. Evolution of entropy and base potential energy: (a) Sensitivity to turbulence diffusivity. (b) Sensitivity to stratification contrast. The initial levels are shown as zero. The thermal entropy is multiplied by a characteristic temperature, which is empirically obtained for each case to match the evolution of entropy with that of BPE.

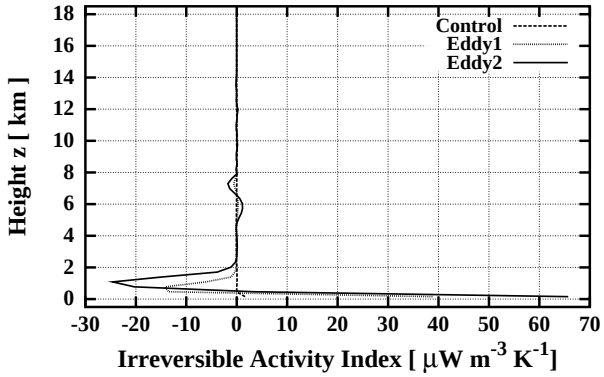

Figure 20. Vertical profiles of irreversible activity index: The irreversible activity index is horizontally averaged over the domain and temporally averaged from model day 15 to day 16.

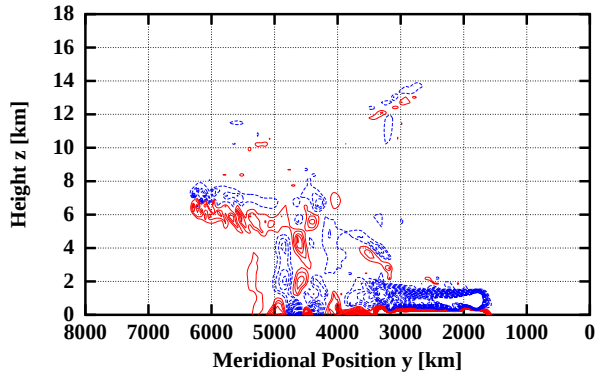

Figure 21. Zonally avaraged irreversible activity index: Red (solid) and blue (dashed) lines indicate positive and negative contours respectively. Contour levels are from $\pm$ 5 to $\pm$ 100 μ W m^{-3} K^{-1} with 5 μ W m^{-3} K^{-1} intervals. The activity is obtained as temporal average from model day 15 to day 16 of Eddy2.